Superconductor Science and Technology

PAPER

Flux pinning mechanisms and a vortex phase diagram of tin-based inverse opals

IOP Publishing Superconductor Science and Technology
Supercond. Sci. Technol. 32 (2019) 115004 (9pp) https://doi.org/10.1088/1361-6668/ab3db7

Flux pinning mechanisms and a vortex phase diagram of tin-based inverse opals

A A Bykov[1], D M Gokhfeld[2], N E Savitskaya[1], K Yu Terentjev[2], S I Popkov[2], A A Mistonov[3], N A Grigoryeva[3], A Zakhidov[4] and S V Grigoriev[1,3]

[1] Petersburg Nuclear Physics Institute named by B.P. Konstantinov NRC 'KI', Gatchina, Russia
[2] Kirensky Institute of Physics, Federal Research Center KSC SB RAS, Krasnoyarsk, Russia
[3] Saint-Petersburg State University, Saint-Petersburg, Russia
[4] The University of Texas at Dallas Alan G. MacDiarmid NanoTech Institute, Dallas, TX, United States of America

E-mail: redi87@bk.ru

Received 29 May 2019, revised 6 August 2019
Accepted for publication 22 August 2019
Published 23 September 2019

Abstract

Three-dimensional periodic tin structures were synthesized by filling pores in silicon opals with a sphere diameter of 194 nm (Sn190) and 310 nm (Sn300). The samples were examined by the ultra-small-angle x-ray diffraction method, energy dispersive x-ray microanalysis and scanning electron microscopy. It was found that the inverse opal structure consists of tin nanoparticles inscribed in octahedral and tetrahedral pores with diameters of 128 nm and 70 nm for the sample Sn300, and 80 nm and 42 nm for the sample Sn190. The study of the magnetic properties of the samples by SQUID magnetometry showed that magnetization reversal curves exhibit hysteretic behavior. The mechanisms of magnetic flux pinning in the samples depend on the size of the tin nanoparticles. Tin nanoparticles in Sn300 behave like a classical type-I superconductor. The hysteretic behavior of the magnetization reversal curves at low magnetic fields is due to the formation of a network of superconducting contours in Sn300. These superconducting contours effectively trap the magnetic flux. The octahedral tin nanoparticles in Sn190 remain type-I superconductors, but smaller tetrahedral particles behave like type-II superconductors. Type-I and II superconducting particles in Sn190 lead to the coexistence of different mechanisms of flux pinning. These are flux trapping by superconducting contours at low magnetic fields and flux pinning by tetrahedral particles due to the surface barrier at high magnetic fields.

Keywords: tin-based inverse opal, superconductivity, magnetic flux pinning, three-dimensional inverse nanostructures

(Some figures may appear in colour only in the online journal)

1. Introduction

Magnetic flux penetration and trapping in low-dimension superconducting samples and superconducting nanoparticles are strongly dependent on their characteristic sizes [1–3]. One of the first observations of size-dependent modifications of magnetization curves was performed for mercury, which was pressed into porous Vicor glass, by Bean *et al* [4]. Recently, methods have been developed for producing nanostructured superconductors constituted by individual nanoparticles with a size of ~10–100 nm [5–10]. These methods give perspectives for size-regulated composite superconducting materials with controlled magnetic properties. Arrays of Josephson junctions are usually made by lithography [11], and can be used as detectors of charged particles [12] and devices for low-frequency radio communications [13]. Comparable arrays of spatially ordered superconducting nanoparticles are effectively produced by the inclusion of superconducting materials into the opal matrix. Investigations of near-perfect and relatively simple inverse opal-like structures (IOLS) give new perspectives for the creation of various devices. The period of the opal structures a_0 can be changed

over a wide range from hundreds of nanometers to micrometers. In [5, 6, 14–17], nanostructured superconductors based on gallium, indium, lead, bismuth, antimony, Wood's alloy (Bi–Pb–Sn–Cd) and Bi–Sb alloy embedded into the opal matrix with $a_0 = 160$–500 nm have already been investigated. The superconducting properties of such IOLS were found to depend on the characteristic size of the included superconducting particles. The measured magnetization reversal curves have features caused by penetration of the magnetic vortices into pores and into superconducting regions of the realized nanoparticle arrays [6, 17].

The size of the superconducting regions in nanostructured superconductors determines the value of the mean free path of the charge carriers l and hence the coherence length ξ [1]. Reducing the size of the superconducting particles limits l, reduces ξ, and changes the Ginsburg–Landau parameter $\kappa = \lambda_L/\xi$, where λ_L is the London penetration depth. The value of $\kappa = 1/\sqrt{2}$ is the boundary between type-I and II superconductors [18]. Thus, limiting l can lead to a change in the type of superconductivity from I to II.

The shape of the magnetization hysteresis loops can be controlled in nanostructured superconductors by regulation of the particle sizes. Tin is well suited for this purpose, because the Ginsburg–Landau parameter is closer to $1/\sqrt{2}$ for Sn ($\lambda_L = 35$ nm, $\xi = 300$ nm [19]) than for Al or Bi, but not so close as for Pb. In the case of Sn, the transition from the type-I to II superconductivity is sufficiently delayed for detailed consideration. Indeed, in [7, 10] it was shown that in tin nanoparticles embedded into the dielectric matrices varying the pore size from 120 nm to 8 nm changed the superconductivity type. Tin nanoparticles with the size of 120 nm still remain type-I superconductors with a thermodynamic critical field H_c about 305 Oe corresponding to the massive tin [20]. Samples with tin nanoparticle sizes of 58, 18 and 8 nm become type-II superconductors and are characterized by the second critical field $H_{c2} = 1.5$, 20 and 54 kOe, respectively. It should be noted here that although the size range of tin nanoparticles from 60 nm to 120 nm is crucial for possible intertype effects [3], it remains unexplored.

In the present work, detailed results of the synthesis and investigation of three-dimensional periodic tin structures obtained by filling the pores of opals are reported. The opals were constructed from silicon dioxide (SiO_2) spheres with a diameter of 194 nm (denoted Sn190) and 310 nm (denoted Sn300). The sizes of the structural elements of the samples were larger than those in investigation [7], but smaller than those in [10]. This paper is organized as follows. Section 2 presents the results of the structural characterization of tin-based IOLS specimens. The magnetic properties and a discussion of the mechanisms leading to the pinning of the magnetic flux are given in sections 3 and 4. In section 5, the main results are summarized.

2. Investigation of tin IOLS structures

Opal-like matrices were obtained by slow sedimentation of amorphous SiO_2 spheres with diameters of 194 and 310 nm from a monodisperse aqueous colloidal solution [16, 21]. Then the precipitate was dried and annealed at 750 °C. The structure of an ideal opal has a face-centered cubic (fcc) lattice in which the positions are occupied by SiO_2 spheres. The structure parameter is defined as $a_0 = D\sqrt{2}$, where D is the diameter of the SiO_2 spheres. Octahedral and tetrahedral voids formed between the spheres alternate along the $\langle 111 \rangle$ crystallographic directions [22, 23]. Cubes with a size of $5 \times 5 \times 5$ mm^3 were cut from the opal matrix. These cubes were infiltrated with the melted tin metal under applied pressure (the melting point of tin is 231.9 °C). The infiltration was carried out in a piston-cylinder-type apparatus that provides large hydrostatic stresses. A porous template was put in a stainless steel capsule; the capsule was tightly filled with a metal powder and sealed. The infiltration procedure included heating the capsule to a temperature slightly over the melting point of the metal, subjecting it to a pressure of 1–2 kbar for 30 min, and cooling to room temperature under the same pressure. The isostatic pressurization of the melt under mild conditions must exclude distortions of the fragile templates [14, 16]. As result, inverse opal-like tin samples were synthesized. The samples are denoted as Sn190 (for the SiO_2 spheres with a diameter of 194 nm) and Sn300 (for the SiO_2 spheres with a diameter of 310 nm).

The chemical composition of the samples was examined by energy dispersive x-ray microanalysis [24]. The study was performed using a Zeiss Merlin scanning electron microscope equipped with an Inca X-act EDS detector and Oxford Instruments Inca analytical software. The working distance was 10 mm, the beam current was 1 nA, the electron beam acceleration voltage was 10 kV, the image magnification was 200, and the counting time of the spectrum was 50 s. Figure 1 shows the dispersion of the energy spectrum from the selected micro-area of around 40 000 μm^2 for Sn190 and Sn300. Distinct characteristic peaks for ^{8}O, ^{14}Si and ^{50}Sn are clearly observed. For the Sn300 sample the spectral lines corresponding to the light elements of sodium ^{11}Na, chlorine ^{17}Cl and carbon ^{6}C are observed due to the slight contamination of the sample surface with salt; the line of gold ^{79}Au is present in the spectrum due to the electrodes deposited to measure the conductivity of the samples.

Scanning electron microscopy (SEM) images of Sn190 in the plane (100) and Sn300 in the plane (111) are shown in figure 2. It is seen that filling the voids of the opal matrix with tin resulted in small deformations of both the SiO_2 spheres and their spatial order. As a result, the tin nanoparticles in tetrahedral and octahedral voids are connected to each other by thin bridges.

The structural studies of the sample structure were performed with high-resolution x-ray diffraction using compound refractive optics. This method was successfully used to investigate different stacking sequences in opal-like structures based on polystyrene or silicon oxide spheres [21, 25], and in IOLS based on ferromagnetic (Ni, Co) or oxide materials (TiO_2, SiO_2, Fe_2O_3) [22, 23, 26, 27]. The measurements were taken at the DUBBLE BM-26 line in the European Synchrotron Radiation Facility (Grenoble, France). The details of the experimental setup are given in [28]. Briefly, diffraction of the

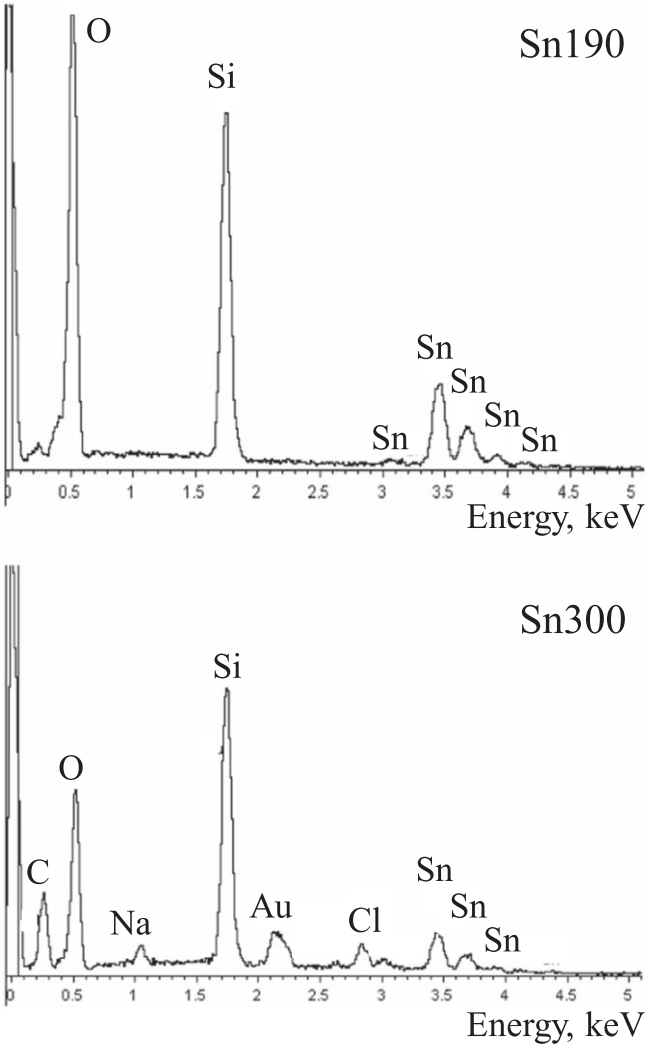

Figure 1. Energy dispersive x-ray microanalysis spectra for samples Sn190 and Sn300.

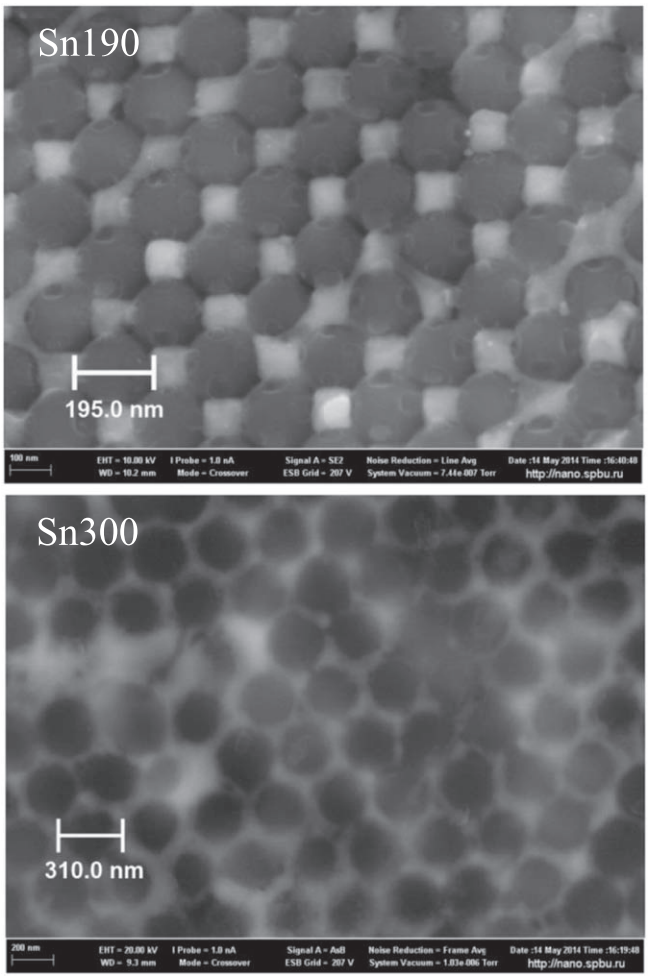

Figure 2. SEM images of Sn190 sample in the plane (100) and Sn300 sample in the plane (111).

monochromatic 13 keV x-ray beam ($\lambda = 0.095$ nm; $\Delta\lambda/\lambda = 2 \times 10^{-4}$) was registered behind the sample at a distance of 7.31 m by a two-dimensional charge-coupled device detector (Photonic Science) with 4008 × 2671 pixels of 9 × 9 μm. The diameter of the x-ray beam was about 500 μm. Rods with a cross-section of 100 × 100 μm^2 and length of about 5 mm were cut from tin IOLS cubes for diffraction experiments. The rods were mounted vertically on a goniometer and rotated in the angle range of 180 degrees with a step of 0.5 degrees around the vertical axis of the rods. The incident synchrotron radiation was directed perpendicular to the long axis of the rods.

The diffraction patterns consist of only first-order Bragg reflections. It indicates an appreciable disturbance in the spatial ordering for both Sn190 and Sn300. Momentum transfer dependences of the total intensity $I(q)$ scattered by the crystallographic plane (202) in Sn190 and Sn300 are plotted in figure 3. These dependences were fitted as the sum of Lorentz and squared Lorentz functions to describe the diffraction maximum and the scattering in the small-angle region, respectively.

Periods $d_{hkl} = 2\pi/q_{hkl}$ of crystallographic planes and, consequently, the lattice constants $a_0 = d_{hkl}\sqrt{h^2 + k^2 + l^2}$ for Sn190 and Sn300 were calculated from the positions of the Bragg maxima with the assumption that the samples have fcc structure. The obtained structural parameters are presented in table 1.

The width of the Bragg maxima (figure 3) can be used to estimate the average crystallite size. The width of the Bragg maximum 202 is $\Delta q_{202} = 11 \times 10^{-4}$ nm^{-1} for Sn190 and $\Delta q_{202} = 7 \times 10^{-4}$ nm^{-1} for Sn300. This corresponds to the sizes of the crystallite L (Sn190) = 5.7 μm and L (Sn300) = 9.0 μm.

Based on the fulfilled structural analysis, it should be concluded that the Sn300 and Sn190 samples consist of tin nanoparticles distributed in the voids of the SiO_2 opal matrix as the fine dispersed inclusions in the form of tetrahedra and octahedra. The vertices of the tin nanoparticles conjoin in the crystallographic directions ⟨111⟩ (figure 4). Given the period of the opal matrix fcc structure, one can precise the diameter D of the SiO_2 spheres and then estimate the sizes of tin nanoparticles as the diameters of the spheres inscribed in the octahedral $D_O = D(\sqrt{2}–1)$ and tetrahedral $D_T = D(\sqrt{1.5} - 1)$ opal matrix voids, and both the length l_C and the diameter of the cylinders $D_C = D\ (2/\sqrt{3}\text{-}1)$ connecting these inscribed spheres (figure 4). The obtained values can be found in table 1. From this

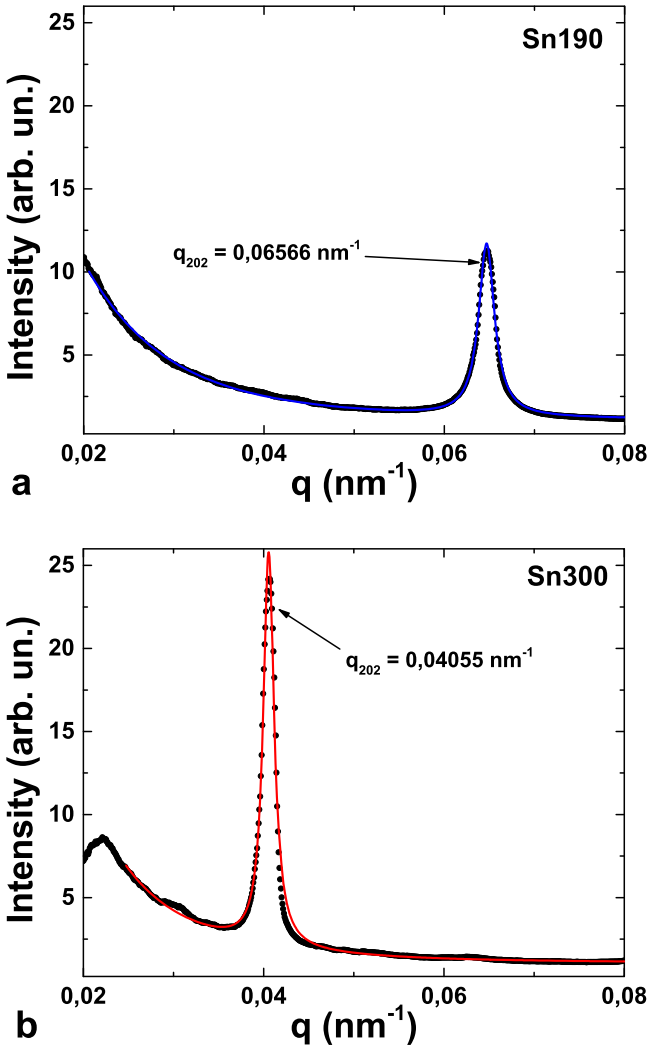

Figure 3. Momentum transfer dependences of the total intensity $I(q)$ scattered by the crystallographic plane (202) in Sn190 (a) and Sn300 (b) samples.

data one can easily obtain the volume fractions of the unit cell occupied by tin and SiO_2. The unit cell volume is $V_{IOLS} = 22.63\ R^3$, the volume occupied by SiO_2 spheres is $V_{SiO2} = 16.76\ R^3$, the volume occupied by tin is $V_{Sn} = 5.87\ R^3$, the volume of the tetrahedra is $V_{tetr} = 0.36\ R^3$, the volume of the octahedra is $V_{oct} = 1.16\ R^3$ and the volume of the cylinder (leg) $V_{legs} = 4.35\ R^3$ where $R = D/2$ is the radius of the SiO_2 spheres. Thus, about 35% of the unit cell volume is occupied by Sn and 65% of the unit cell volume is occupied by SiO_2. The calculations were based on the number of tetrahedra (8), octahedra (4) and cylinders (32) per unit cell. For the investigated samples, the tin frame around each SiO_2 sphere was formed from six octahedra and eight tetrahedra connected by 24 cylinders.

3. Magnetic properties of tin IOLS

The magnetic characteristics of the IOLS were measured in the temperature range from 1.7 K to 5 K by Quantum Design

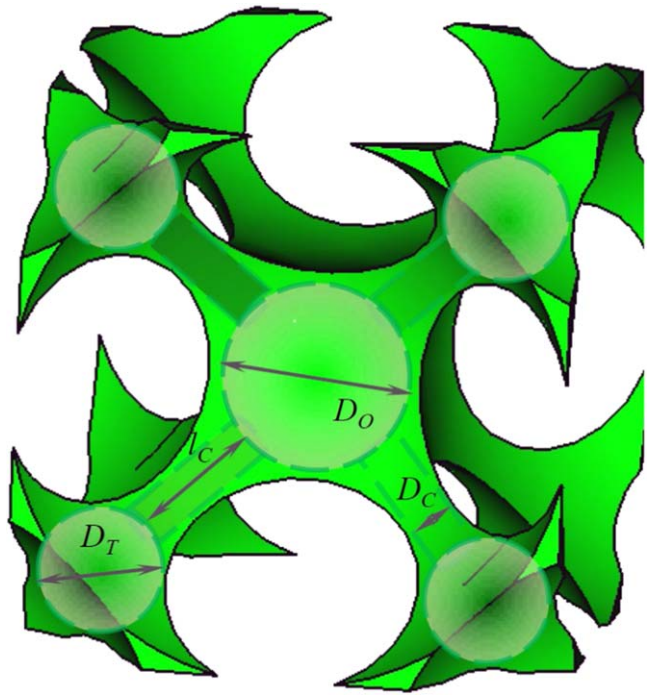

Figure 4. The unit cell of the IOLS. The octahedral and tetrahedral tin nanoparticles with diameter D_O and D_T, respectively, and cylinders of length l_c and cross section D_c, connecting the spheres, are shown schematically.

SQUID MPMS magnetometer at the Technical University of Braunschweig and by Quantum Design PPMS-9 magnetometer at Kirensky Institute of Physics, Krasnoyarsk. Magnetization curves were measured at several temperatures up to magnetic fields of 5 T. The samples for magnetic measurements had sizes of $4 \times 3 \times 1\ mm^3$ and $1 \times 1 \times 0.5\ mm^3$ and masses of 33.31 mg and 5.65 mg for Sn300 and Sn190, respectively.

Figure 5 shows the temperature dependences of the magnetization M of Sn300 and Sn190 at $H = 20$ Oe. The data show clear diamagnetic behavior. Diamagnetic shielding becomes maximal at temperatures near 2.6 K and 3.0 K for Sn300 and Sn190, respectively. The superconductor critical temperature T_c was identified as the temperature where the magnetization reaches 50% from its minimal value. $T_c = 3.47 \pm 0.02$ K for Sn300 and $T_c = 3.62 \pm 0.02$ K for Sn190. The values of T_c for both Sn300 and Sn190 are lower than $T_c = 3.69$ K for the bulk tin. The reduction of T_c may be related to impurities and quantum fluctuations [1].

Figure 6(a) demonstrates the $M(H)$ curves for Sn300 at $T = 1.87$ K. The critical field H_c of Sn300 is about the same as the H_c of bulk tin [20]. Therefore, despite the small size of the tetrahedra and octahedra, Sn300 remains a type-I superconductor. Figure 6(b) shows the temperature dependences of the critical fields marked in figure 6(a). Some characteristic features can be highlighted on the $M(H)$ curves of Sn300. At the initial magnetization the $M(H)$ dependence decreases linearly. Conspicuously, the external field induces the superconducting currents in a tin carcass on the sample surface. These currents screen the inside of the sample. An initial

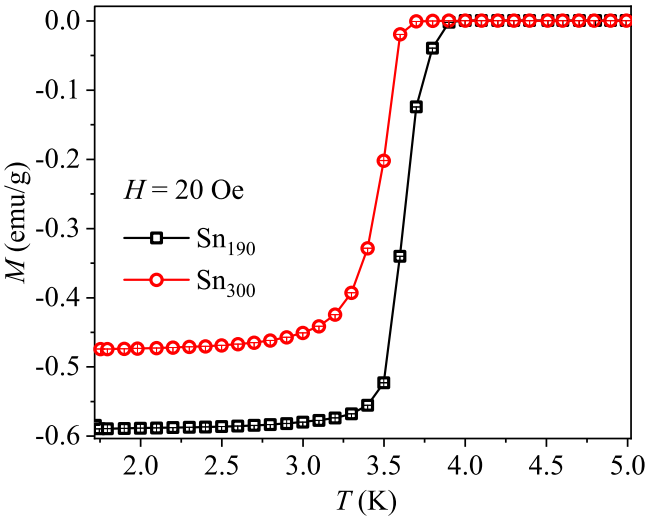

Figure 5. Temperature dependence of the magnetization of the samples Sn300 and Sn190.

linear decrease of the magnetization field is related to Meissner state magnetization (region I in figure 6(b)). However, the slope of the magnetization reversal curve $M = -\alpha H$ corresponds to $\alpha = 0.67$. It means that only $2/3$ of the sample volume is shielded from the external magnetic field.

The observed lower critical field H'_{c1} is the point at which the virgin $M(H)$ dependence begins to deflect from the linear line. Further evolution of the magnetization is governed by weak linked superconducting contours formed at the tin framework around the SiO_2 spheres. The superconducting contours are formed by the connected tin nanoparticles. At $H'_{c1} < H < H'_{c2}$ the magnetic flux penetrates through the SiO_2 spheres (region II in figure 6(b)). The sharp kink in $M(H)$ dependence at $H = H_p$ is associated with the full penetration field. The critical field H'_{c2} and region III in figure 6(b) correspond to the breakdown of the screening current circulation in the superconducting contours. In the field above H_c the entire sample enters a state with normal conductivity (region IV in figure 6(b)). When the magnetic field decreases from H_c to H'_{c2}, the current circulation in the superconducting contours is restored. The entered magnetic flux appears to be trapped by the superconducting contours [29]. Due to flux trapping, the magnetization of the tin carcass has a reversible behavior and $M(H)$ dependence has hysteresis in the field range of $-H'_{c2} < H < H'_{c2}$.

The $M(H)$ dependences for Sn190 look like the hysteresis magnetization loop of a type-II superconductor (figure 7(a)) [30]. The temperature dependences of the critical fields for Sn190 are presented in figure 8(b).

The linear dependence of $M(H)$ at $0 < H < H'_{c1}$ with a slope of $\alpha \approx 0.9$ indicates almost complete shielding of the internal part of the sample from the external magnetic field due to the superconducting currents induced on the sample surface (figure 7(a)). Similar to Sn300, the field H'_{c1} corresponds to the first critical field of Sn190 (Meissner phase, region I in figure 8(b)). As the field increases, $H > H'_{c1}$, the magnetic flux begins to penetrate into the silicate spheres. In the range of $H'_{c1} < H < H_{oct}$ the magnetization is governed by weak linked superconducting contours formed around the SiO_2 spheres (region II in figure 7(b)). The diamagnetic response and superconductivity disappear at H higher than the upper critical field H_{c2} (region VI in figure 7(b)). Also, forward and reverse $M(H)$ curves are merged at $|H| \geqslant H_{c2}$. From figure 7(a)), the value of H_{c2} is obviously much larger than the value of the critical field for bulk tin $H_c = 305$ Oe [13].

The large value of H_{c2} indicates that the mean free path of the electrons significantly decreases with the decreasing sizes of tin particles, which leads to a decrease of the coherence length ξ and, as a consequence, to the manifestation of type-II superconductor properties. The effective coherence length is determined as:

$$\xi = \sqrt{\frac{\Phi_0}{2\pi\mu_0 H_{c2}(0)}} \quad (1)$$

where Φ_0 is the magnetic flux quantum, μ_0 is the magnetic constant, and $H_{c2}(0)$ is the upper critical field at a temperature close to absolute zero. Given $H_{c2}(0) \approx 3000$ Oe (figure 8(b)), the effective coherence length of Sn190 is about 33 nm. The size of the tetrahedra is close to this value of ξ. It can be assumed that the tetrahedral particles in Sn190 turn out to be type-II superconductors. A mixed state is realized in these particles at $H_{oct} < H < H_{c2}$ (region III in figure 7(b)). The magnetic flux penetrates into the tetrahedra in the form of Abrikosov vortices up to $H = H_{c2}$. Octahedral particles that are larger than 33 nm remain type-I superconductors. Superconductivity in the octahedral particles is suppressed at $H > H_{oct}$. Note that the values of H_{oct} for Sn190 are close to H_c for Sn300 at similar temperatures (figures 6(b), 7(b)). This fact also speaks in favor of our hypothesis about the presence of type-I tin nanoparticles in Sn190.

The $M(H)$ curve for Sn190 has hysteretic behavior in the whole range of the fields $-H_{c2} < H < H_{c2}$. Two factors determine this hysteresis. In the high fields $H > H_{oct}$ the irreversible magnetization is associated only with the pinning of magnetic vortices in the small tin particles, i.e. with the presence of a surface barrier [25]. In the low fields $H < H_{oct}$, as for the case of Sn300, the magnetic flux is pinned by superconducting contours.

4. Discussion

The sample magnetization depends on the demagnetizing factor and the volume fractions of tin and SiO_2 spheres. For an ideal fcc opal structure corresponding to Sn300:

$$M_{sample} = 0.26M_{Sn} + 0.74M_{SiO2}, \quad (2)$$

where M_{SiO2} is the magnetization of the superconducting contours around the silicate matrix, and M_{Sn} is the magnetization of the tin carcass. The effective demagnetizing factor of the sample at $0 < H < H_m$ is

$$N_1 \approx 1 - H_m/H_c, \quad (3)$$

Table 1. Structural parameters of Sn190 and Sn300 samples according to the results of ultra-small-angle diffraction of synchrotron radiation.

q_{111}, nm^{-1}	d_{111}, nm	q_{202}, nm^{-1}	d_{202}, nm	a_0, nm	D, nm	D_O, nm	D_T, nm	D_C, nm	l_C, nm
Sample Sn190									
0.040(2)	157.08(2)	0.065(1)	96.66(1)	274(5)	194(5)	80(2)	42(2)	30(2)	45(2)
Sample Sn300									
0.025(2)	251.33(2)	0.040(1)	157.07(1)	438(5)	310(5)	128(2)	70(2)	48(2)	67(2)

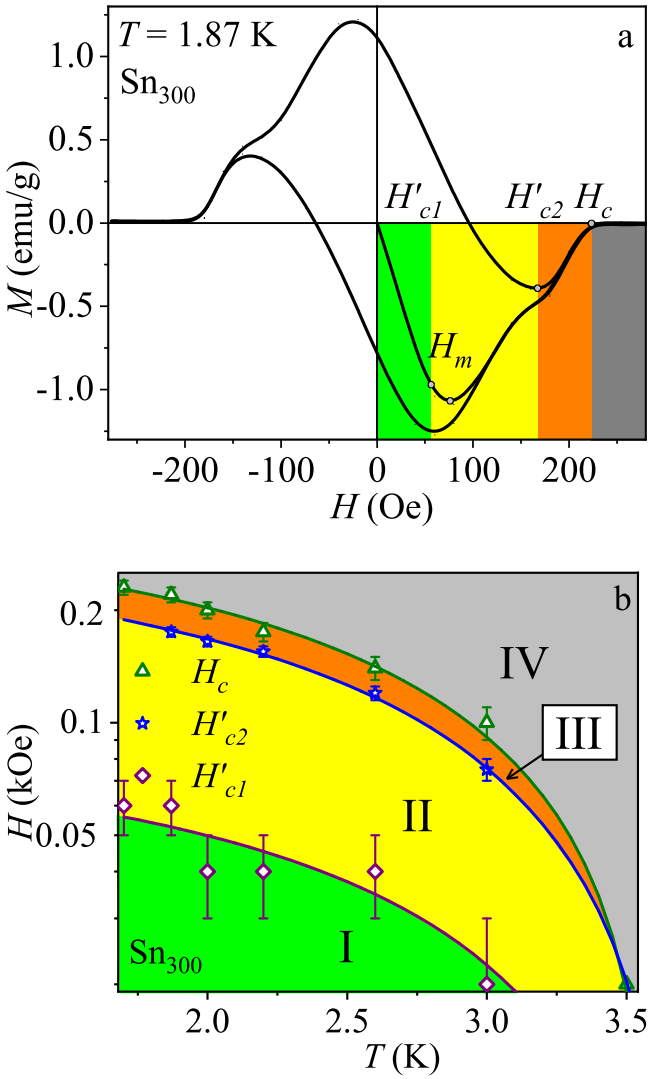

Figure 6. (a) The $M(H)$ curve for Sn300 at $T = 1.88$ K. (b) Temperature dependences of the critical fields for Sn300. Lines are the approximation functions of $H = H_0\,[1–(T/T_c)^2]$, where $T_c = 3.72$ K. Roman numerals mark the different states described in the text.

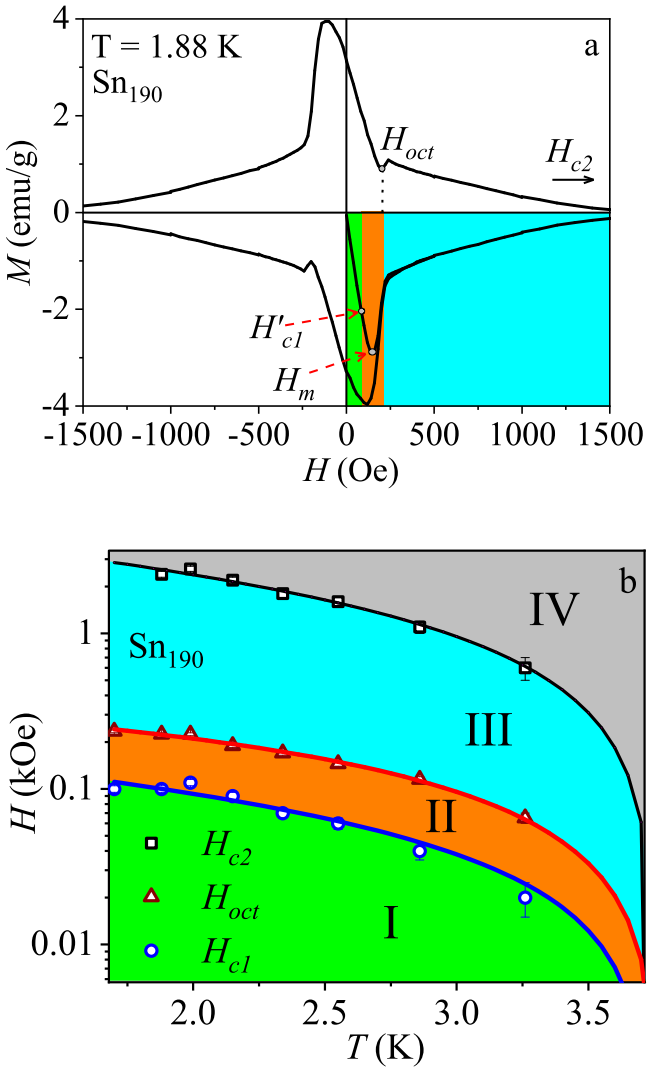

Figure 7. (a) The $M(H)$ curve at $T = 1.88$ K for Sn190. (b) Temperature dependences of the critical fields for Sn190. Lines are the approximation functions $H = H_o[1–(T/T_c)^2]$, where $T_c = 3.62$ K. Roman numerals mark the different states described in the text.

since in the low magnetic fields the magnetic flux hardly penetrates into the tin carcass. At the high magnetic fields $H'_{c2} < H < H_c$ the demagnetizing factor of the sample is

$$N_2 \approx M_{H=H'c2}/(0.26(H_c - H'_{c2}) + M(H'_{c2})), \qquad (4)$$

since the magnetization of the sample is determined predominantly by the magnetization of the tin carcass. In the intermediate values of field $H_m < H < H'_{c2}$ the contribution of the sample regions with the demagnetizing factor N_1 decreases, and the contribution of the regions with N_2 increases with the increasing of the magnetic field.

Figure 8 shows the calculated magnetization curve for the Sn300 sample. To calculate the magnetization the contributions of N_1 and N_2 for each value of the field were chosen in such a way that the magnetization curves were crosslinked without features. The satisfactory coincidence of the simulation results and the experimental $M(H)$ dependence confirms the correctness of our above assumptions regarding the magnetic behavior of Sn300.

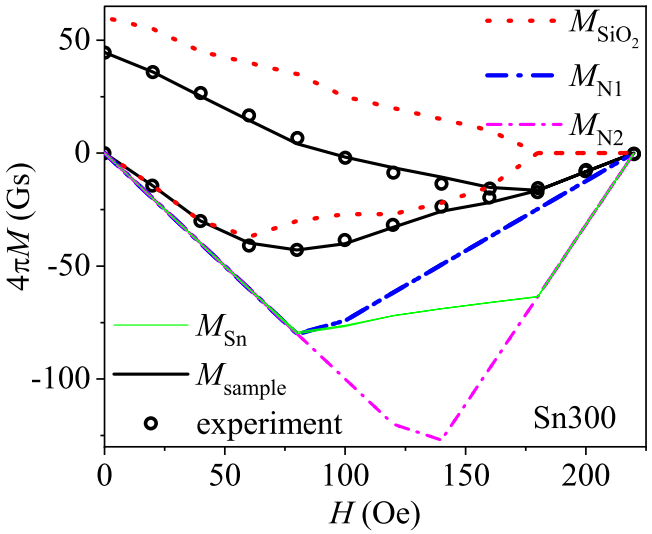

Figure 8. Experimental and theoretical $M(H)$ dependences for Sn300 at $T = 1.88$ K. The empty circles are the experimental data. The dotted line is the theoretical magnetization of the superconducting contours around silicate spheres M_{SiO2}. The dash-dotted line is the theoretical magnetization of the tin carcass, which corresponds to the magnetization with N_1 (equation (3)) in the low fields, and to the magnetization with N_2 (equation (4)) in the high fields. The solid black line is the total theoretical magnetization M_{sample} (equation (2)).

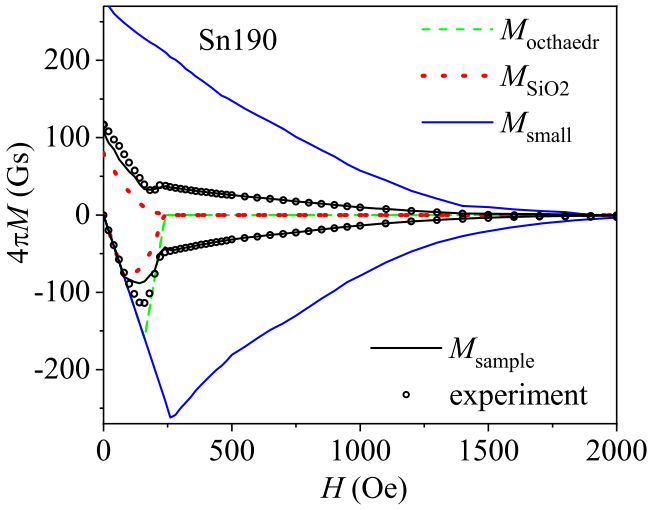

Figure 9. Experimental and theoretical $M(H)$ dependences for the Sn190 sample at $T = 1.99$ K.

Figure 9 shows the magnetization curve of Sn190 calculated taking into account the volume fraction of tin particles and the superconducting contours around SiO_2 spheres:

$$M_{sample} = 0.21M_{small} + 0.05M_{oct} + 0.74M_{SiO2}, \quad (5)$$

where M_{SiO2} is the magnetization of the superconducting contours around the silicate matrix, M_{oct} is the magnetization of the octahedral particles, and M_{small} is the magnetization of smaller (tetrahedra) particles.

The magnetization of the octahedral particles was calculated on the assumption that they are type-I superconductors with a demagnetizing factor $N_1 = 1/3$. The magnetization of the smaller particles (tetrahedra) was calculated on the assumption that they are type-II superconductors having upper critical field H_{c2}. For simulating the magnetization of the superconducting contours, it was taken into account that the magnetic field enters them at $H = H'_{c1}$. Then, at $H'_{c1} < H < H_{oct}$, superconducting currents circulate around the SiO_2 spheres. The insignificant quantitative discrepancy between the experimental data and the theoretical curve (figure 9) may be explained by inaccurate values of the sample density and the volume fractions of tin particles and the SiO_2 matrix (equations (2) and (5)), which were calculated for the perfect fcc structure of IOLS.

Thus, tin nanoparticles in the size range from 42–128 nm were treated and the transition between type-I and II superconductivity in IOLS was traced. The observed intertype-like magnetization curves of Sn190 were due to the occurrence of type-I and II tin nanoparticles in the sample [18]. We found that superconducting contours, which were realized due to a percolation between tin nanoparticles in the samples, provided effective trapping of the magnetic flux, even in the sample with type-I particles. The same pinning of superconducting contours occurs in other samples with current percolation (e.g. [5–9]). Carbon-coated nanoparticles [6] do not have current percolation and magnetization hysteresis.

Oscillations of the magnetic moment due to the forming of individual fluxoid states [31] were not observed in the measured magnetization curves, in contrast to [6]. Lower temperatures are possibly required to observe these magnetization oscillations in the samples.

5. Conclusion

Spatially ordered tin superconductors with an inverted opal structure were synthesized. The pores of the silicon opals with sphere diameters of 194 nm (Sn190) and 310 nm (Sn300) were filled with tin. The samples were investigated by ultra-small-angle x-ray diffraction, energy dispersive x-ray microanalysis, SEM and SQUID magnetometry methods. It was shown that IOLS consists of octahedral and tetrahedral tin nanoparticles inscribed in opal pores with diameters of 128 nm and 70 nm for Sn300, and 80 nm and 42 nm for Sn190.

The critical field H_c of Sn300 is close to the thermodynamic critical field of bulk tin, and therefore Sn300 is a type-I superconductor despite the small sizes of its tetrahedral and octahedral particles. However, the magnetization reversal curve has irreversibility (hysteresis). Hysteretic behavior in the field range of $-H'_{c2} < H < H'_{c2}$ is due to pinning of the magnetic flux on superconducting contours around SiO_2 spheres.

The Sn190 sample has magnetization hysteresis loops like a type-II superconductor. We suppose that the included tetrahedral tin particles with a size of 42 nm behave like type-II superconductors, and the included tin octahedra with a size

of 80 nm remain type-I superconductors. Thus, in Sn190, type-I and type-II superconductivities coexist, which leads to a nontrivial pinning of the magnetic flux. For the first time, the transition of the flux pinning mechanisms is observed with the magnetic field increasing. At low fields the magnetic flux is trapped by superconducting contours. At high fields the magnetic flux pinning works due to the surface barrier in the small tetrahedra tin particles.

Controlled modifications of magnetization curves are desirable for applications. IOLS gives the possibility to set the required shapes of magnetization hysteresis loops. The ratio of the smaller and larger nanoparticles affects different regions of the magnetization curve. Arrays of self-consistent weak linking circuits can be created by a rather simple synthesis of IOLS.

Acknowledgments

The authors are grateful to Dr D A Balaev for the discussions, Dr A V Chumakova for the ultra-small-angle x-ray diffraction experiments, Dr Dirk Menzel for SQUID measurements, I S Dubitskiy for structural illustrations, and the Interdisciplinary Resource Center for Nanotechnology of St. Petersburg State University for the SEM measurements.

The work was supported by the Russian Foundation for Basic Research, project no. 17-72-10067.

ORCID iDs

A A Bykov https://orcid.org/0000-0001-6561-6015
D M Gokhfeld https://orcid.org/0000-0001-9049-9973

References

[1] Bose S and Ayyub P 2014 A review of finite size effects in quasi-zero dimensional superconductors *Rep. Prog. Phys.* **77** 116503
[2] Córdoba-Camacho W Y, da Silva R M, Vagov A, Shanenko A A and Aguiar J A 2016 Between types I and II: intertype flux exotic states in thin superconductors *Phys. Rev.* B **94** 054511
[3] Córdoba-Camacho W Y, da Silva R M, Vagov A, Shanenko A A and Aguiar J A 2018 Quasi-one-dimensional vortex matter in superconducting nanowires *Phys. Rev.* B **98** 174511
[4] Bean C P, Doyle M V and Pincus A G 1962 Synthetic high-field, high-current superconductor *Phys. Rev. Lett.* **9** 93–4
[5] Shamshur D V, Chernyaev A V, Fokin A V and Romanov S G 2005 Electrical conductivity and superconductivity of ordered indium-opal nanocomposites *Phys. Solid State* **47** 1927–36
[6] Aliev A E, Lee S B, Zakhidov A A and Baughman R H 2007 Superconductivity in Pb inverse opal *Physica C* **453** 15–23
[7] Ciou Y S, Lee M K, Charnaya E V, Tien C, Chang L J, Kumzerov Y A and Samoylovich M I 2013 Superconductivity in Sn nanocomposites *Supercond. Sci. Technol.* **26** 055009
[8] Moura K O, Pirota K R, Béron F, Jesus C B R, Rosa P F S, Tobia D, Pagliuso P G and Lima O F 2017 Superconducting properties in arrays of nanostructured β-gallium *Sci. Rep.* **7** 15306
[9] Zeng X L, Karwoth T, Koblischka M R, Hartmann U, Gokhfeld D, Chang C and Hauet T 2017 Analysis of magnetization loops of electrospun nonwoven superconducting fabrics *Phys. Rev. Mater.* **1** 044802
[10] Shani L, Kumar V B, Gedanken A, Shapiro I, Shapiro B Y, Shaulov A and Yeshurun Y 2018 Type-I superconductivity in carbon-coated Sn nano-spheres *Physica C* **546** 6–10
[11] Bogomolov V N, Kumzerov Y A, Romanov S G and Zhuravlev V V 1993 Josephson properties of the three-dimensional regular lattice of the weakly coupled nanoparticles *Physica C* **208** 371–84
[12] Di G D, Poccia N, Lankhorst M, Gatti C, Buonomo B, Foggetta L, Marcelli A and Hilgenkamp H 2017 A novel particle/photon detector based on a superconducting proximity array of nanodots *J. Supercond. Nov. Magn.* **30** 359–63
[13] Reagor D, Fan Y, Mombourquette C, Jia Q and Stolarczyk L 1997 A high-temperature superconducting receiver for low-frequency radio waves *IEEE Trans. Appl. Supercond.* **7** 3845–9
[14] Kozlov M E, Murthy N S, Udod I, Khayrullin I I, Baughman R H and Zakhidov A A 2007 Preparation, structural, and calorimetric characterization of bicomponent metallic photonic crystals *Appl. Phys.* A **86** 421–5
[15] Charnaya E V, Tien C, Lin K J, Wur C S and Kumzerov Y A 1998 Superconductivity of gallium in various confined geometries *Phys. Rev.* B **58** 467–72
[16] Zakhidov A A, Baughman R H, Iqbal Z, Cui C, Khayrullin I, Dantas O, Marti J and Ralchenko V G 1998 Carbon structures with three-dimensional periodicity at optical wavelengths *Science* **282** 897–901
[17] Lungu A, Bleiweiss M, Amirzadeh J, Saygi S, Dimofte A, Yin M, Iqbal Z and Datta T 2001 Superconductivity in nanostructured lead *Physica* C **349** 1–7
[18] Ginzburg V L and Landau L D 1950 K voprosu sverkhprovodimosti *J. Exp. Theor. Phys.* **20** 1064
[19] Tinkham M 2004 *Introduction to Superconductivity* (*Dover Books on Physics*) vol 1 2nd edn (New York: Dover)
[20] Roberts B W 1976 Survey of superconductive materials and critical evaluation of selected properties *J. Phys. Chem. Ref. Data* **5** 581–822
[21] Eliseev A A *et al* 2009 Determination of the real structure of artificial and natural opals on the basis of three-dimensional reconstructions of reciprocal space *JETP Lett.* **90** 272–7
[22] Grigoryeva N A *et al* 2011 Magnetic topology of Co-based inverse opal-like structures *Phys. Rev. B* **84** 064405
[23] Sinitskii A, Abramova V, Grigorieva N, Grigoriev S, Snigirev A, Byelov D V and Petukhov A V 2010 Revealing stacking sequences in inverse opals by microradian x-ray diffraction *Europhys. Lett.* **89** 14002
[24] Goldstein J I, Newbury D E, Echlin P, Joy D C, Lyman C E, Lifshin E, Sawyer L and Michael J R 2003 *Scanning Electron Microscopy and X-ray Microanalysis* (Boston, MA: Springer US)
[25] Napolskii K S *et al* 2010 Fabrication of artificial opals by electric-field-assisted vertical deposition *Langmuir* **26** 2346–51
[26] Grigoriev S *et al* 2009 Structural and magnetic properties of inverse opal photonic crystals studied by x-ray diffraction, scanning electron microscopy, and small-angle neutron scattering *Phys. Rev.* B **79** 045123
[27] Chumakova A V, Valkovskiy G A, Mistonov A A, Dyadkin V A, Grigoryeva N A, Sapoletova N A, Napolskii K S, Eliseev A A, Petukhov A V and Grigoriev S V 2014 Periodic order and defects in Ni-based inverse opal-like crystals on the mesoscopic and atomic scale *Phys. Rev. B* **90** 144103

[28] Borsboom M *et al* 1998 The Dutch Belgian beamline at the ESRF *J. Synchrotron Radiat.* **5** 518–20

[29] Bykov A A, Terent'ev K Y, Gokhfeld D M, Savitskaya N E, Popkov S I and Petrov M I 2018 Superconductivity on interfaces of nonsuperconducting granules La_2CuO_4 and $La_{1.56}Sr_{0.44}CuO_4$ *J. Supercond. Nov. Magn.* **31** 3867–74

[30] Senoussi S 1992 Review of the critical current densities and magnetic irreversibilities in high Tc superconductors *J. Phys. III* **2** 1041–257

[31] Geim A K, Dubonos S V, Palacios J J, Grigorieva I V, Henini M and Schermer J J 2000 Fine structure in magnetization of individual fluxoid states *Phys. Rev. Lett.* **85** 1528–31